The Astrophysical Journal, 891:49 (10pp), 2020 March 1 https://doi.org/10.3847/1538-4357/ab711c

Upward Overshooting in Turbulent Compressible Convection. II. Simulations at Large Relative Stability Parameters

Tao Cai[1,2]
[1] State Key Laboratory of Lunar and Planetary Sciences, Macau University of Science and Technology, Macau, People's Republic of China; tcai@must.edu.mo, caitao7@mail.sysu.edu.cn
[2] School of Mathematics, Sun Yat-sen University, No. 135 Xingang Xi Road, Guangzhou, 510275, People's Republic of China
Received 2019 August 9; revised 2020 January 22; accepted 2020 January 27; published 2020 March 3

Abstract

In this paper, we present the results of three-dimensional numerical simulation of upward overshooting in turbulent compressible convection at large relative stability parameter S. Similar to the previous simulations at small S, we find that the convectively stable zone can be partitioned into three layers: the thermal adjustment layer, the turbulent dissipation layer, and the thermal dissipation layer. Despite of this similarity, there exist significant differences in several aspects. First, for small S, the thermal structure is altered considerably near the interface between the convectively unstable and stable zones. For extremely large S, the thermal structure is only slightly changed. Second, the overshooting distance decreases at small S, but it can increase when S is large enough. Third, for small S, the fluid motions tend to be less active when S increases. However, the fluid motions can be more active when S is large enough. We find that the structure of counter cells has a significant impact on the penetration depth.

Unified Astronomy Thesaurus concepts: Stellar interiors (1606); Stellar cores (1592); Stellar convective zones (301); Stellar structures (1631); Hydrodynamical simulations (767)

1. Introduction

Convective core overshooting is an important but unresolved problem in stellar structure and evolution. The material mixing induced by core overshooting can significantly affect the life time of stars at the main-sequence stage. In one-dimensional stellar evolution models, the extent of overshooting distance is usually estimated by the Schwarzschild criterion with a free parameter $\alpha_{\rm ov}$ (e.g., Shaviv & Salpeter 1973; Maeder 1975; Roxburgh 1978), or alternatively modeled by a diffusive process with a free diffusion coefficient $f_{\rm ov}$ (Freytag et al. 1996; Herwig et al. 1997). However, empirical results on calibration of overshooting parameters indicate that neither $\alpha_{\rm ov}$ nor $f_{\rm ov}$ is a constant (Woo & Demarque 2001; Deheuvels et al. 2016; Claret & Torres 2017, 2018, 2019). The uncertainty of overshooting parameter values requires further investigations. From an analytic model, Zahn (1991) predicted that the overshooting zone includes two layers: a nearly adiabatic penetrative layer and a thermal adjustment overshooting layer. Zahn's theory was confirmed in the two-dimensional (2D) simulation of penetration below a convection zone (Hurlburt et al. 1994). They found that the penetration distance decreases with the relative stability parameter S, with scalings $\delta \sim S^{-1}$ in the nearly adiabatic layer and $\delta \sim S^{-1/4}$ in the thermal adjustment layer, respectively. However, the scalings have only been partially confirmed (lack of the nearly adiabatic penetrative layer) in the three-dimensional (3D) simulations (Brummell et al. 2002), probably because the filling factor in 3D simulations is much smaller for the penetrative plumes compared to the 2D simulations. Scalings of δ on S were also examined in other numerical simulations (Singh et al. 1995; Rogers & Glatzmaier 2005; Pal et al. 2007; Korre et al. 2019), but all these simulations focused on the penetration below a convection zone. It has been known that upward overshooting is significantly different from downward overshooting (Chan et al. 2010). One of the key questions about the stellar model is how to define the overshooting boundary (Deng & Xiong 2008). For downward overshooting, the penetration depth is usually defined at (or close to) the first zero of the kinetic energy flux in the stable layer (e.g., Hurlburt et al. 1994; Singh et al. 1995; Brummell et al. 2002). However, the kinetic energy is not an appropriate indicator for upward overshooting (Chan et al. 2010). Through material mixing experiments, Chan et al. (2010) have advised to use zeros of the vertical velocity correlation (with the vertical velocity at the interface) as indicators for the extent of overshooting distance. The experiments also reveal that the small-scale turbulent dissipative process plays an important role in mixing materials in the overshooting zone (Chan et al. 2010). A similar small-scale turbulent dissipative process has been discovered in other simulations (Arnett et al. 2015; Rogers & McElwaine 2017), while the explanation of its driving mechanism is different. For example, Arnett et al. (2015) attributed its driving mechanism to the shear instability; Rogers & McElwaine (2017) explained it as a result of an internal gravity wave; and Chan et al. (2010) favored the explanation of counter cells.

Apart from 3D simulations, progress on the 1D theoretical analysis of the turbulent convection model in the overshooting region has been made by Zhang & Li (2012). In their analysis, they partitioned the stable region into three layers: an efficient turbulent heat transfer layer, a turbulent dissipation layer, and an inefficient thermal dissipation layer (Zhang & Li 2012). In a previous paper (Cai 2020), we have performed three-dimensional simulations on upward overshooting of turbulent compressible convection at small S. The result has shown promising agreement with the analysis of Zhang & Li (2012), when the first and second zero-points are used as indicators for the measurement of overshooting distances (Chan et al. 2010). The scalings of overshooting distance on S were also investigated. Although no obvious uniform scalings were identified, it has been found that the overshooting distance tends to decrease with S. In this paper, we extend the work of

Table 1
Parameters of Numerical Simulations

Case	$N_x \times N_y \times N_z$	S	μ	$F_{\rm tot}$	Ra	Pr	$\langle v'' \rangle_{cz}$	Re	Pe	δ_1	δ_2
D1	$512^2 \times 301$	250	1.0×10^{-4}	0.00075	1.34×10^9	1.0	0.065	1818	1818	0.105	0.330
D2	$512^2 \times 301$	500	1.0×10^{-4}	0.00075	1.34×10^9	1.0	0.063	1758	1758	0.075	0.255
D3	$512^2 \times 301$	1000	1.0×10^{-4}	0.00075	1.34×10^9	1.0	0.062	1742	1742	0.055	0.205
D4	$512^2 \times 301$	2000	1.0×10^{-4}	0.00075	1.34×10^9	1.0	0.061	1714	1714	0.050	0.175
D5	$512^2 \times 301$	4000	1.0×10^{-4}	0.00075	1.34×10^9	1.0	0.061	1717	1717	0.045	0.170
D6	$512^2 \times 301$	8000	1.0×10^{-4}	0.00075	1.34×10^9	1.0	0.060	1677	1677	0.040	0.175
D7	$512^2 \times 301$	16000	1.0×10^{-4}	0.00075	1.34×10^9	1.0	0.060	1686	1686	0.045	0.200
D8	$512^2 \times 301$	100000	1.0×10^{-4}	0.00075	1.34×10^9	1.0	0.060	1708	1708	0.060	0.395

Note. N_x, N_y, and N_z are the numbers of grid points in x-, y-, and z-directions, respectively. S is the relative stability parameter. μ is the dynamic viscosity. $F_{\rm tot}$ is the total flux. Ra is the averaged Rayleigh number. Pr is the averaged Prandtl number. $\langle v'' \rangle_{cz}$ is the averaged rms velocity. Re is the averaged Reynolds number. Pe is the averaged Péclet number. δ_1 is the distance measured by the first zero of velocity correlation. δ_2 is the distance measured by the second zero of velocity correlation. All the averaged values are taken both temporally and spatially in the convection zone.

Cai (2020), by performing 3D numerical simulations of upward overshooting at large S.

2. The Model

We perform 3D numerical simulations on turbulent compressible convection of an ideal gas (the ratio of specific heats $\gamma = 5/3$) in a Cartesian box with a convectively stable layer (layer 2) sitting above an unstable layer (layer 1). The initial distribution of the gas (the temperature T, the density ρ, and the pressure P) is in a piecewise polytropic state (initial temperature structure is piecewise linear) with $m_1 = 1.4985$ in the layer 1, and $m_2 > 1.5$ in the layer 2 (m_2 is a constant in the layer 2). We normalize all the physical variables by the temperature, density, pressure, and the height at the interface between the layer 1 and layer 2. The gravity $g = (m_i + 1)\eta_i = 4.997$ is set to be a constant throughout the computational domain, where $\eta_i = -(dT/dz)_i$ and $i \in \{1, 2\}$ is the layer index. Similar to the previous study (Cai 2020), we define the relative stability parameter $S = (m_2 - m_{\rm ad})/(m_{\rm ad} - m_1)$, the Prandtl number $\Pr(z) = c_p \mu/\kappa_i$, the Rayleigh number $\mathrm{Ra}(z) = [1 - (\gamma - 1)m_i](m_i + 1)\eta_i^2 \rho^2 \Pr(z)/(\gamma \mu^2)$, the Reynolds number $\mathrm{Re}(z) = \rho v'' L_{1z}/\mu$, and the Péclet number $\mathrm{Pe}(z) = \mathrm{Re}(z) c_p \mu/\kappa_i$, where $m_{\rm ad} = 1.5$ is the polytropic index of adiabatic polytrope, $c_p = 2.5$ is the specific heat capacity at constant pressure, κ_i is the thermal diffusive coefficient, μ is the dynamic viscosity, L_{1z} is the height of the layer 1, and v'' is the rms velocity. In the simulations, we keep the total flux $F_{\rm tot} = 1.5\kappa_1 g/(m_1 + 1) = \kappa_2 g/(m_2 + 1)$ a constant throughout the computational domain. Note that the heat conductivity κ_i is a piecewise constant function across the domain. In the initial settings, all the flux is transported by heat conduction in layer 2, but only two-thirds of the flux is transported by heat conduction in layer 1. The simulation parameters are listed in Table 1. The computational domain is periodic in both horizontal directions, and impenetrable and stress-free at the top and bottom. The temperature is fixed at the top, and a constant flux is supplied at the bottom. We solve a full set of compressible hydrodynamic equations by a semi-implicit mixed finite-difference spectral method (Cai 2016). The numerical settings and methods are similar to those used in Cai (2020). The major difference is that the relative stability parameters are much larger in this work ($S \in [1, 7]$ in Cai (2020), while $S \in [250, 100{,}000]$ in this paper).

3. Results

3.1. Layer Structure in the Convectively Stable Zone

An earlier study on upward overshooting demonstrated that the first and second zero-points of velocity correlation (with the velocity at the interface) are good indicators for measuring overshooting distance (Chan et al. 2010). In the previous simulations on upward overshooting at small S (Cai 2020), based on these indicators, we have partitioned the convectively stable zone into three layers: the thermal adjustment layer (mixing both entropy and material), the turbulent dissipation layer (mixing material but not entropy), and the thermal dissipation layer (mixing neither entropy nor material). This partition is still valid in our simulations on upward overshooting at large S. A comparison of layer structures among Zahn (1991), Zhang & Li (2012), and Cai (2020) is given in the Appendix. A detailed discussion on how to define the extent of overshooting distance is reported in Cai (2020). Figure 1 shows the snapshots of the contours of the temperature perturbation and vertical velocity for the case D1. The interface between the convectively unstable and stable zones ($z = 1.0$), the first zero of velocity correlation ($z = 1.105$), and the second zero of velocity correlation ($z = 1.33$) are illustrated by dashed lines. From the contours, we see that strong and narrow downward drafts are formed at the top of the convection zone. On the contrary, the upward drafts are generally weak and broad when they arrive at the top of the convection zone. Despite the weakness of the upward drafts, the figure clearly shows that they can pass through the interface, penetrate into the convectively stable layer, and turn around after reaching the first zero-point. The vertical velocity decays rapidly after the upward draft penetrates into the convective stable zone. The temperature perturbation, on the other hand, becomes negative before the upward draft reaches the first zero-point. Unlike the vertical velocity, the magnitude of the temperature perturbation in this penetrative layer is comparable to that in the convectively unstable layer (see Figure 2(a)). Since the temperature perturbation is anticorrelated with vertical velocity, the enthalpy flux F_e ($=\overline{\rho c_p v_z T_1}$, where overbar denotes spatial and temporal averages) is negative in this region (see Figure 2(c)). To balance the negative transport of F_e, the thermal structure is adjusted accordingly so that the temperature gradient ∇ exceeds the radiative temperature gradient $\nabla_{\rm rad}$ (see Figure 3(b)). The upward drafts can hardly cross the first zero-point. Although the vertical velocity is small above the first zero-point, the temperature perturbation and the

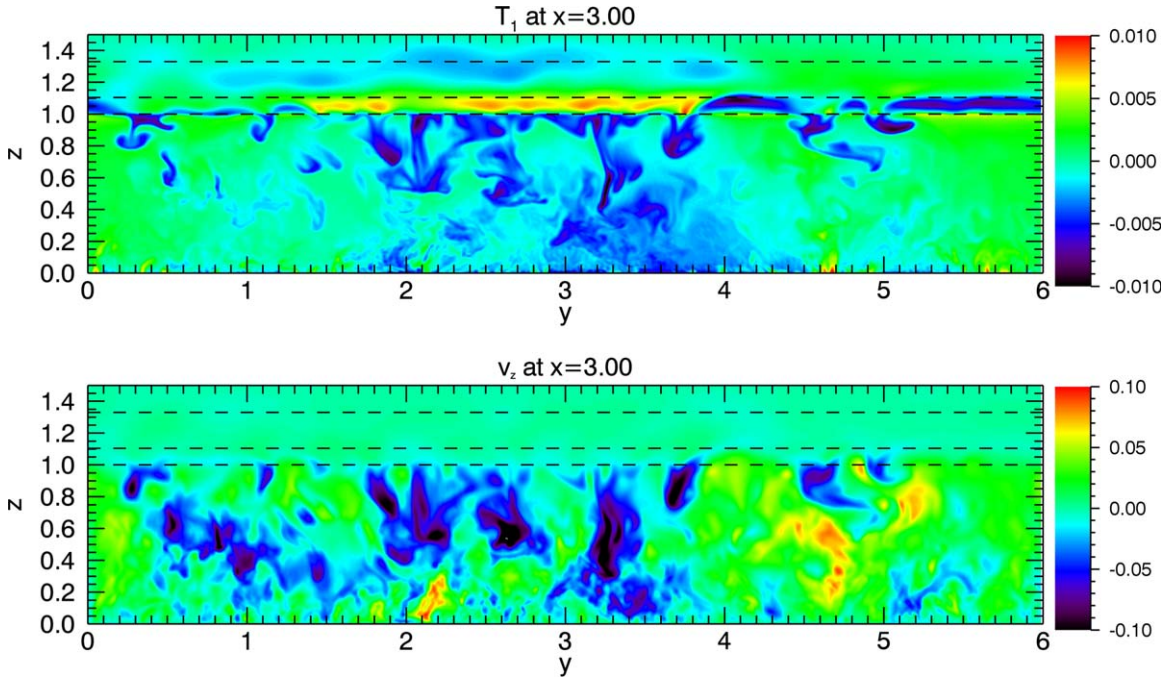

Figure 1. Snapshots of the flow structure (vertical cut at $x = 3.0$) for the case D1. The upper panel shows the contour of the temperature perturbation, and the lower panel shows the contour of the vertical velocity. The dashed lines indicate the interface between convectively unstable and stable zones ($z = 1.0$), the first zero of velocity correlation ($z = 1.105$), and the second zero of velocity correlation ($z = 1.33$), respectively. The bright (dark) color denotes positive (negative) values.

horizontal velocity are nonnegligible, at least in the region below the second zero-point (see Figure 2(a)). The enthalpy flux is negligible in this region (see Figure 2(c)), but the mixing is still active by the turbulent dissipation. Above the second zero-point, the Péclet number $\mathrm{Pe_{Hp}} \lesssim 1$ (see Figure 2(e)), where $\mathrm{Pe_{Hp}} \lesssim 1$ uses local pressure scale height as the characteristic length) and the fluid motions are dominated by thermal diffusion.

Figure 2 shows the statistical results of case D1 ($S = 250$ on the left panel) and case D7 ($S = 16000$ in the right panel). From the asymptotic solution of a Reynolds stress model, Zhang & Li (2012) suggested to use the location of the peak of T_1'' (the rms turbulent temperature perturbation) as the boundary of the penetrative layer (or the thermal adjustment layer in our paper). In our simulations, the peak of T_1'' is close to the first zero-point for the case $S = 250$ (Figure 2(a)). However, the peak of T_1'' seems closer to the interface, rather than the first zero-point, for the case $S = 16{,}000$ (Figure 2(b)). Hence, the peak of T_1'' might not be the best proxy for identifying the boundary of the thermal adjustment layer. From Figures 2(a) and 2(b), we find that the first zero-point is almost located at the inflection point of T_1''. Thus we suggest to use the inflection point of T_1'' as the indicator for the boundary of the thermal adjustment layer. It has to be mentioned that the inflection point of T_1'' works better at high S cases. Zhang & Li (2012) have made the assumption that the diffusive term of T_1'' is unimportant in the overshooting zone. It would be more consistent with their assumption if we choose the inflection point of T_1'' as the proxy. Figures 2(c) and 2(d) show the enthalpy flux F_e, the diffusive flux $F_d - F_{\rm ad}$ (where $F_d = -\kappa \partial \overline{T}/\partial z$ and $F_{\rm ad} = -\kappa(\partial \overline{T}/\partial z)_{\rm ad}$), and the kinetic fluxes $F_k = 0.5\overline{\rho v_z (v_h^2 + v_z^2)}$ for D1 and D7, respectively. As mentioned before, there is a dip of F_e in the thermal adjustment layer. From these two subfigures, we see that the absolute value of the dip minimum increases with S. Thus, it is expected that the thermal structure in this layer will deviate more from the initial static state for the case D7 than D1. However, compared with D1, Figure 3(b) clearly shows that D7 deviates less from the static state (see the wiggles above the interface in Figure 3(b)). The reason for this is that the thermal diffusivity $\kappa_2 = F_{\rm tot}[S(m_{\rm ad} - m_1) + m_{\rm ad} + 1]/g$ is much larger in case D7. Thus a small adjustment of thermal structure can lead to significant change in fluxes. Figures 2(e) and 2(f) plot both Pe and $\mathrm{Pe_{Hp}}$. Apparently, the second zero-point approximately locates at the position of $\mathrm{Pe_{Hp}} \approx 1$ (the variation is within a factor of $0.5 \sim 2.0$). It is consistent with the assumption made on the turbulent dissipation layer in the Reynolds stress model (Zhang & Li 2012). The second zero is located a little bit away from the location $\mathrm{Pe_{Hp}} = 1$ (being above for the low S case and below for the high S case). There are two possible reasons for this. One is that the characteristic length scale of Pe should be associated with the length scale of turbulent motions. It can be different for different cases. The second reason is that the characteristic velocity of Pe is evaluated by rms velocity, while the second zero tends to capture the extreme events.

3.2. The Extent of Overshooting Distance

The last two columns of Table 1 give the overshooting distances measured by the first (δ_1) and second (δ_2) zero-points, respectively. To better illustrate the result, we plot $\log(\delta_1)$ and $\log(\delta_2)$ against $\log(S)$ in Figure 3(a). From the figure, we see that δ_1 or δ_2 first decreases, and then increases with S (U-shape). It is different from our previous simulation result at small S, where only a decreasing trend was discovered (Cai 2020). It is counterintuitive that the overshooting distance can increase with S. Here we discuss possible explanations by considering first the thermal adjustment layer. In our previous simulation (Cai 2020), we deduced a relationship between δ_1

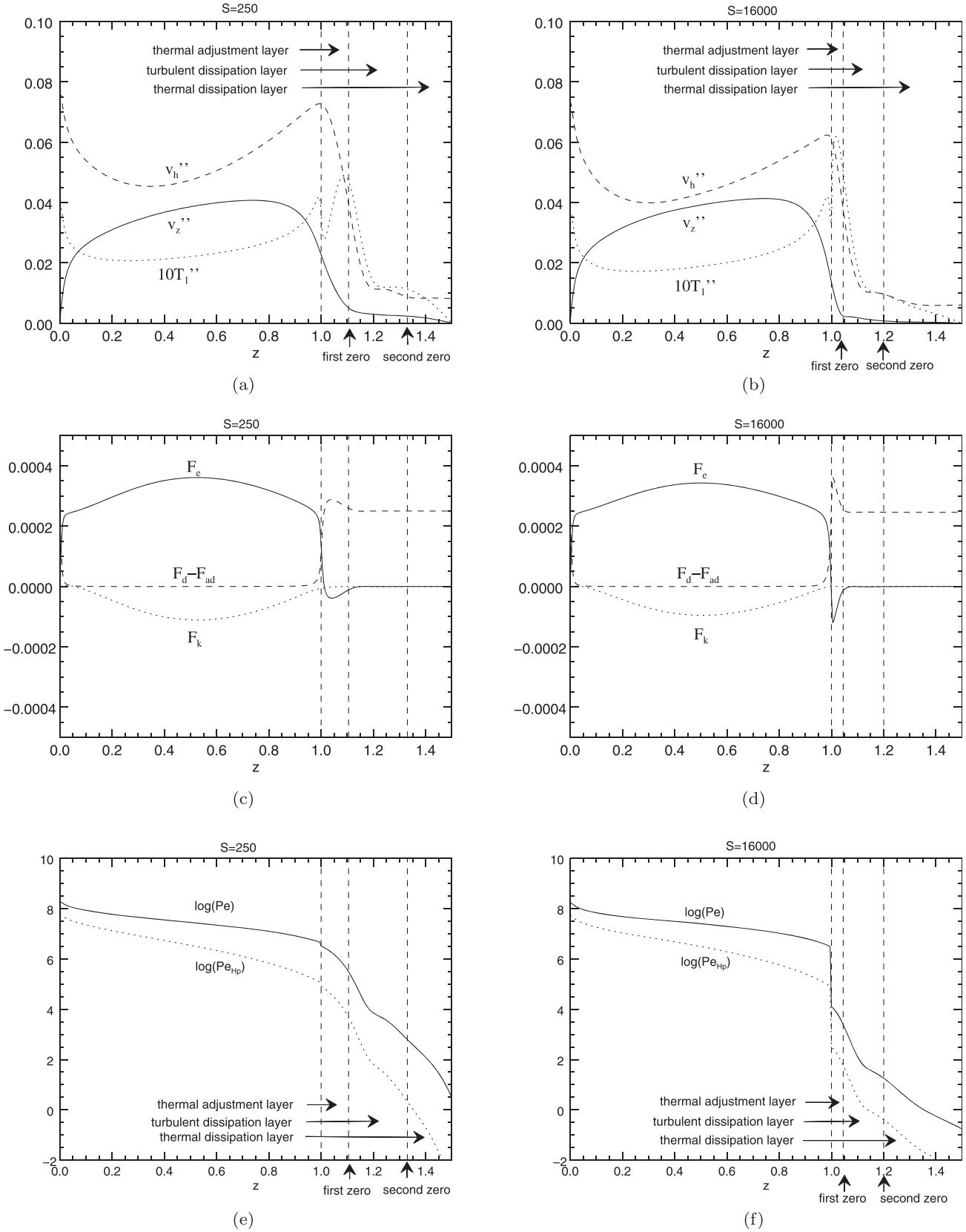

Figure 2. Statistical results of the cases D1 (left panel) and D7 (right panel). Panels (a) and (b) show the rms vertical velocity v_z'', horizontal velocity v_h'', and temperature perturbation ($10T_1''$). Panels (c) and (d) show the enthalpy flux F_e, the diffusive flux $F_d - F_{\rm ad}$, and the kinetic energy flux F_k. The adiabatic flux $F_{\rm ad}$ is deducted from the diffusive flux. Panels (e) and (f) show the profiles of the Péclet numbers Pe and $\rm Pe_{Hp}$. Instead of L_{1z}, $\rm Pe_{Hp}$ uses the local pressure scale height as the characteristic length.

and W_* (the exit vertical velocity at the interface):

$$W_*^2 \approx \frac{g^2}{c}(\nabla - \nabla_{\rm ad})\delta_1^2 = \frac{g^2}{c}\frac{m_{\rm ad} - m_1}{m_{\rm ad}+1}\frac{S}{S(m_{\rm ad}-m_1)+(m_{\rm ad}+1)}\delta_1^2, \quad (1)$$

where c is the asymmetry coefficient. The exit velocity W_* is calculated as the rms vertical velocity of upward drafts at the interface. To obtain this relationship, we have made the assumption that $\nabla - \nabla_{\rm ad}$ is almost a constant in the thermal adjustment layer. It can be seen from Figure 3(b) that this assumption is reasonable in our simulations, especially when S is large. Equation (1) infers that δ_1 can be affected by the thermal structure ($\nabla - \nabla_{\rm ad}$), the asymmetry coefficient (c), and the exit vertical velocity at the interface (W_*). First, we consider the effect of the thermal structure. From Figure 3(b) we notice that the absolute value of $\nabla - \nabla_{\rm ad}$ increases with S. However, Equation (1) implies that δ_1 decreases with $|\nabla - \nabla_{\rm ad}|$. Thus the increase of δ_1 is not due to the effect of thermal structure. Second, we consider the effect of the asymmetry coefficient. According to the definition in Zahn (1991), the asymmetry coefficient c is related to the triple moment of the vertical velocity. In our calculation, we find that c varies too much in the overshooting zone. However, the filling factor is more stable. Thus it is more appropriate to compare filling factors, instead of asymmetry coefficients among different cases. Figure 3(c) plots the filling factors at the interface for different cases. The filling factor first decreases, and then increases with S. Despite that the filling factor shows a similar trend with δ_1, its variation (max/min ~1.1) is too small to explain the significant change of δ_1 across different cases. Third, we consider the effect of the exit velocity at the interface. Although the root mean average velocity $\langle v'' \rangle_{cz}$ in the convection zone is almost the same (see Table 1), the exit vertical velocity at the interface is quite different (Figure 3(d)). It has a U-shape, and its variation (max/min ~1.7) is comparable to that of δ_1 (max/min ~ 2.6). Thus we conclude that the exit vertical velocity is the key factor affecting δ_1.

Now we discuss the extent of the turbulent dissipation layer. As shown in Figures 2(e) and 2(f), the boundary of the turbulent dissipation layer is located at the position of $\mathrm{Pe_{Hp}} \sim 1$. From our previous work (Cai 2020), $\mathrm{Pe_{Hp}}$ is of the following form:

$$\mathrm{Pe_{Hp}} = \frac{c_p p v''}{F_{\rm tot}(m_2+1)}. \quad (2)$$

Let $\mathrm{Pe_{Hp}} \sim 1$, the boundary of the turbulent dissipation layer (or δ_2) can be inferred from the value of $p(z)$. The above equation indicates that δ_2 can be affected by m_2 and v''. In our simulation, m_2 varies by two orders of magnitude from 1.875 to 151.5. It is easy to find that δ_2 decreases with m_2 from the above equation. Thus the trend of δ_2 seen in Figure 3(a) cannot be explained only by m_2. Figures 3(e) and (f) plot the averaged vertical and horizontal velocities in the convectively stable zone, respectively. We see that both the averaged vertical and horizontal velocities have U-shapes, similar to the shape of δ_2. Since the horizontal velocity is several times larger than the vertical velocity, δ_2 is mainly affected by the horizontal velocity. It is interesting to note that the fluid motions can be more active in the stable layer when S is large enough. In the simulations of downward overshooting (Brummell et al. 2002; Rogers & Glatzmaier 2005), the case without the stable zone is assumed to be equivalent to $S \to \infty$. For the upward overshooting, however, they are completely different.

To better understand why the overshooting distance increases with S when S is large, we consider two possible mechanism: the shear instability and the counter cell. Figures 4(a) and 4(b) plot the vertical and horizontal velocities of the cases D4–D8 in the convectively stable zone. The velocity profiles are quite similar in the cases D4–D7. However, both the horizontal and vertical velocities are stronger in the convectively stable zone for case D8. In stars, it has been proposed that the material mixing could be induced by the shear instability (Zahn 1992; Maeder 1995). Linear stability analysis has shown that the shear instability occurs when the Richardson number Ri is smaller than a critical value $\mathrm{Ri_c} = 1/4$ (Howard 1961; Miles 1961). Here we define the Richardson number Ri as:

$$\mathrm{Ri}(z) = N^2 \Big/ [\overline{(\partial v_x/\partial z)^2 + (\partial v_y/\partial z)^2}], \quad (3)$$

where $N = \sqrt{g(\nabla_{\rm ad} - \nabla)/H_p}$ is the Brunt–Väisälä frequency, and the overline represents the average value taken both temporally and horizontally. Figure 4(c) shows Ri for the cases D4–D8. From the figure, we see that all the Richardson numbers are above the critical value. The situation does not change even when the effects of the Péclet number (Zahn 1992; Maeder 1995) and the horizontal integral scale of turbulence (Prat & Lignières 2014) are taken into account. Considering the effect of thermal dissipation, Zahn (1992) suggested to use $\mathrm{RiPe} < 1/4$ as the instability criteria. Maeder (1995) improved the result and suggested to use $\mathrm{RiPe}/(6+\mathrm{Pe}) < 1/4$ as the instability criteria. In the overshooting zone, the Péclet number is greater than 1. It can be easily shown that the shear instability could take place in the overshooting zone if $\mathrm{Ri} < 7/4$. Figure 4(c) shows that Ri is much larger than this value. Prat & Lignières (2014) used a horizontal turbulent length scale $\ell = 2\pi \int_0^\infty E(k)k^{-1}dk \Big/ \int_0^\infty E(k)dk$ to calculate the Péclet number. Figures 4(e)–(f) present the result on the evaluated horizontal turbulent length scale. ℓ is much larger than H_p. The Péclet number would be even higher if ℓ is used as the characteristic length. As a result, it is unlikely for the shear instability to take place in the convectively stable zone. Now we consider the possibility of the counter cell. Figure 4(d) shows the anisotropic degree ($\omega = v_z^2/(v_x^2+v_y^2+v_z^2)$) in the convectively stable zone. If the counter cell is important, we would expect that the local minimum points of ω are correlated to the cell nodes. The cells nodes are the barriers to prevent the material from mixing. From Figure 4(d), we can infer that there is one counter cell in the thermal adjustment layer for all the cases. The case is different above the thermal adjustment layer. The figure clearly shows that two counter cells (one extends to the top boundary of the box) exist above this layer in case D4. The cell node between these two cells is approximately at the boundary of the turbulent dissipation layer. Similar counter cells are shown in the cases D5 and D6, but the location of the cell node is subtle. We expect that these two cells would merge

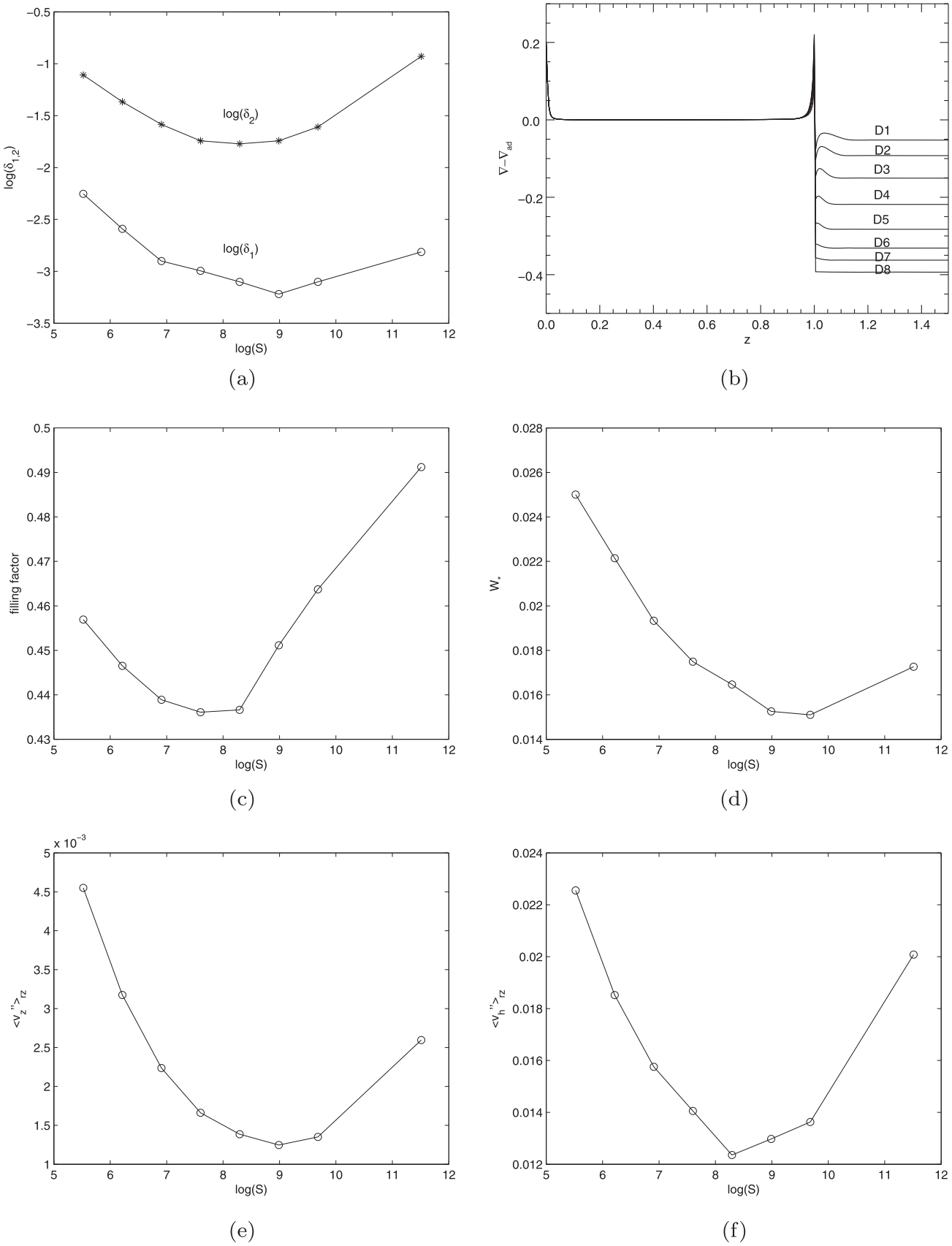

Figure 3. (a) Overshooting distances δ_1 and δ_2 as functions of log(S). (b) The profiles of the super-adiabatic temperature gradient $\nabla - \nabla_{\rm ad}$ for cases D1–D8. (c) The filling factor at the interface for cases D1–D8. (d) The exit vertical velocity at the interface for cases D1–D8. (e) The averaged rms vertical velocity for cases D1–D8. (f) The averaged rms horizontal velocity for cases D1–D8. The average is taken in the convectively stable zone for (e) and (f).

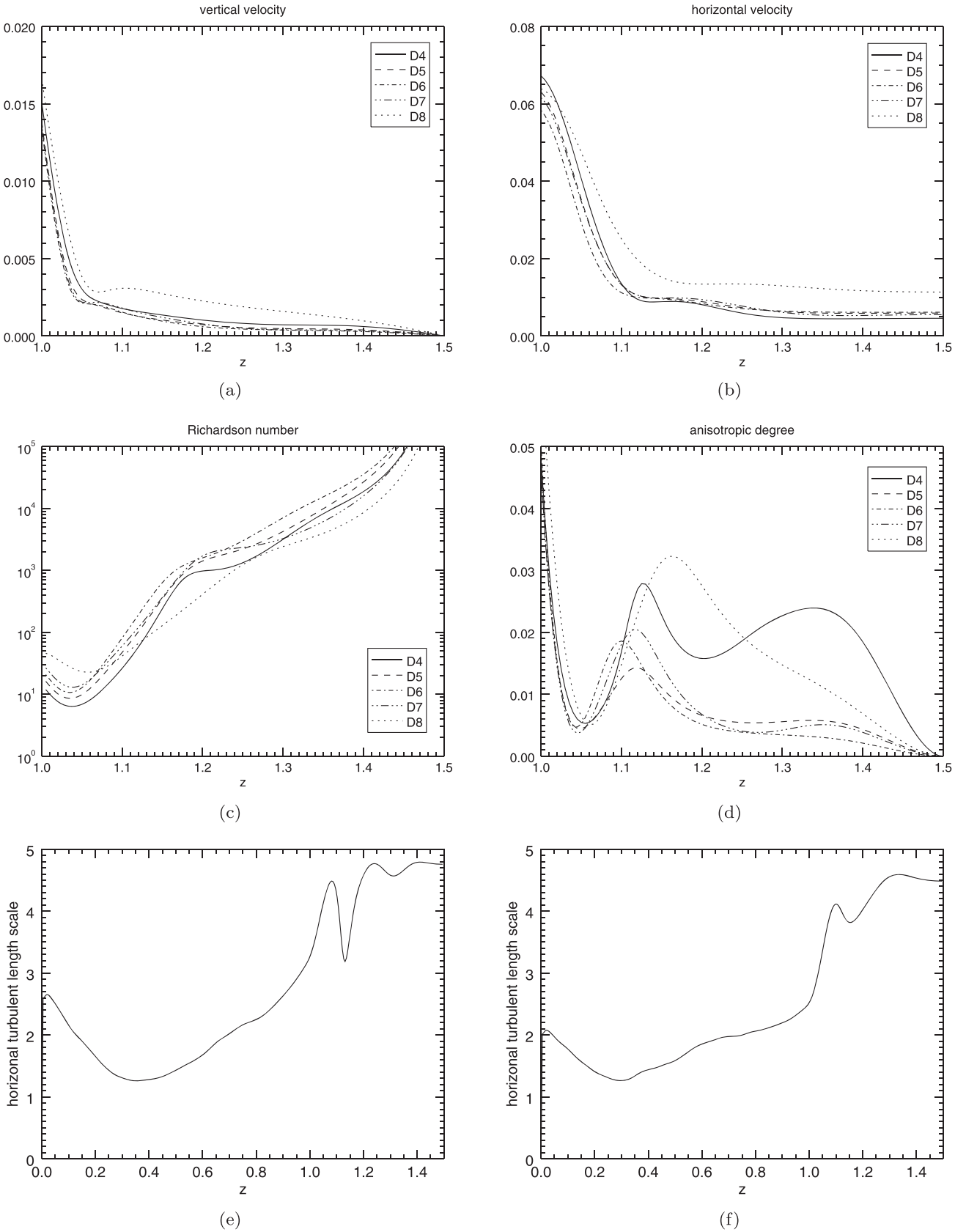

Figure 4. (a) The rms velocity as a function of the depth. (b) The rms horizontal velocity as a function of the depth. (c) The Richardson number as a function of the depth. (d) The anisotropic degree as a function of the depth. (e) The horizontal turbulent length scale for case D4. (f) The horizonal turbulent length scale for case D7.

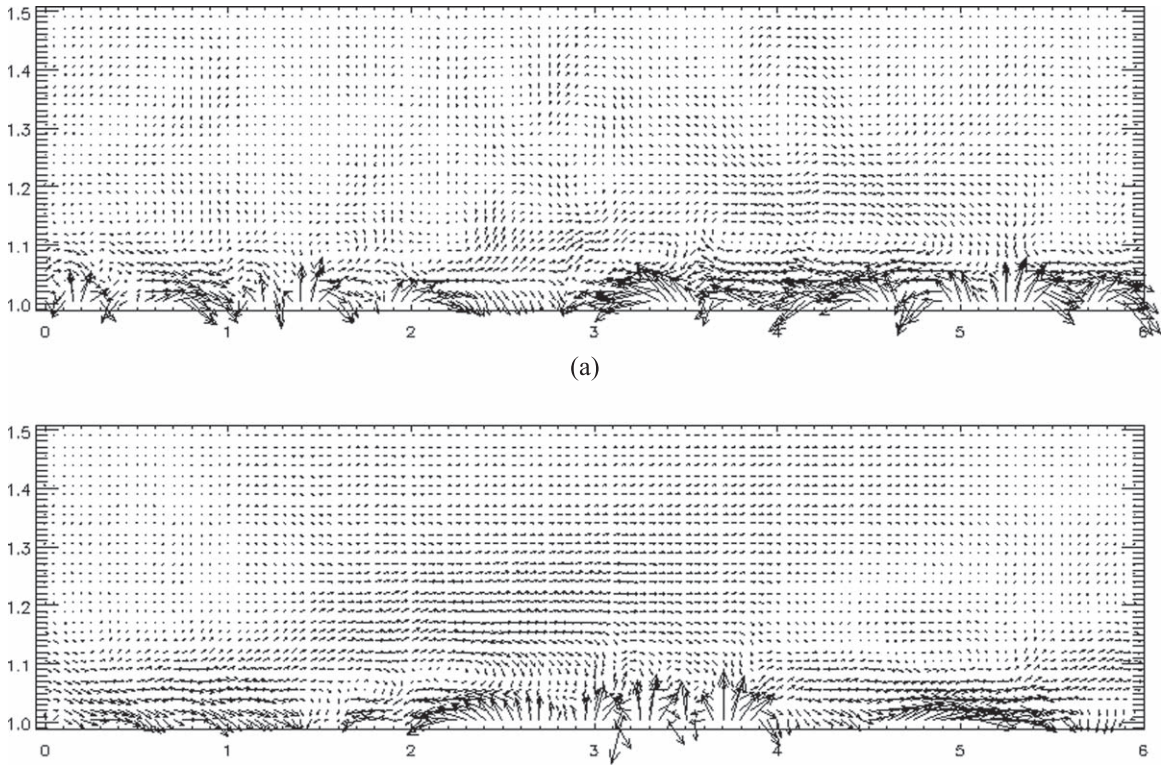

Figure 5. Velocity field at the vertical cut plane $x = 3$. Only the convectively stable zone is displayed. (a) Case D4. (b) Case D7.

when S further increases. For cases D7 and D8, the profile of ω decreases all the way to the top boundary. This indicates that only one counter cell exists and extends all the way to the upper boundary of the box. Once the materials cross the upper boundary of the thermal adjustment layer, they can reach much deeper places through the motion of this large counter cell. The mixing process will be slowed down when the materials enter into the thermal dissipation layer. The counter cells are also confirmed in the profile of velocity field (Figure 5). As a result, we conclude that the counter cells have a significant impact on the extent of the turbulent dissipation layer.

The recent work of Korre et al. (2019) performed 3D simulations on downward overshooting for Boussinesq flow with the stability parameter in the range of $S \in [2, 100]$. Apart from the different settings on geometry and background structure, their work shares some similarities with ours. First, both works use the correlations of vertical velocities as the proxy of the penetrative distance. The zeros of the velocity correlation function tend to pick out the effect of the strongest plume rather than the average effect. In their work, they have reported that the depth measured by the first zero-point of the velocity correlation is close to the depth of thermal mixing. It agrees well with the result of our simulations. Second, their estimated overshooting distance follows scaling laws with $\delta \sim S^{-0.5}$ when the transition region between the unstable and stable zone is thin. In our simulations, the estimated scaling is $\delta_1 \sim S^{-0.47}$ if only cases D1–D3 with relatively smaller S are considered. It is close to their estimations. Third, both the studies use the Péclet number as the proxy to define the boundary of the overshooting layer. Despite these similarities, there are also some differences. For example, in our simulations the turbulent dissipation layer is much wider than the thermal adjustment layer, while the opposite result was reported in their simulations. This is probably because different velocity and length scales are used in the calculation of the Péclet number. It is anticipated that this discrepancy would be diminished if the same scales are used. It seems that the Peclet number should be quoted using a length scale associated with turbulent motions. A calibration of parameters on turbulent Reynolds stress models shows that the vertical turbulent length scale is about $1.2H_p$ (the parameter is calibrated by the data of auto-correlation of vertical velocity in the convection zone; the detailed calibration method can be found in Cai 2018). The vertical turbulent length scale is very close to the H_p. Thus it is reasonable to use H_p as characteristic length scale when evaluating the P'eclet number.

4. Summary

We have performed three-dimensional simulations on the upward overshooting of turbulent compressible convection at large S. Using the zero-points of velocity correlation as indicators, we partition the above convectively stable zone into three layers: the thermal adjustment layer, the turbulent dissipation layer, and the thermal dissipation layer. The layer structure is similar to what we have obtained in the previous simulations on upward overshooting at small S (Cai 2020). Despite of this similarity, there are differences in several aspects. First, the change of thermal structure is different. At small S, the thermal structure is altered considerably in the thermal adjustment layer. At extremely large S, however, the thermal structure is only slightly changed. Second, the extent of the overshooting distance obeys different laws on S. At small S, the extent of overshooting distance decreases with S. For the large S, on the other hand, it first decreases, and then increases

with S. The overshooting distance highly depends on the exit vertical velocity at the interface. Although the averaged velocity in the convection zone is almost the same, the exit vertical velocity can be largely different. Third, the averaged velocity in the convectively stable zone shows different patterns. At small S, the magnitude of velocity decreases with S. For the large S, on the contrary, the magnitude of velocity can even increase when S is large enough. We have considered two possible arguments for why the penetration depth can increase with S: the shear instability and the counter cells. The Richardson number in the convectively stable zone is larger than the typical critical value. Thus it is unlikely for the shear instability to drive the turbulent mixing in the overshooting zone. On the other hand, the argument of counter cells seems to be able to explain this phenomenon. The upward drafts tend to disperse horizontally before reaching the interface. Higher S will lead to higher horizontal velocity of the upward drafts. As they penetrate into the stable zone, they contain more energy on driving counter cells (Chan et al. 2010). These counter cells, in turn, will have feedback on the velocities. One important consequence is that the number of counter cells formed in the convectively stable zone can be changed. As the cell nodes form the barrier of material mixing, the structure of the counter cells has a significant impact on the penetration depth. A similar driving mechanism called "differential heating" has been discussed in Andrássy & Spruit (2015). When radiative diffusion transports a temperature fluctuation into the convectively stable zone, the resulting perturbation can trigger a weak flow with several layers of overturning cells. It has to be mentioned that our model adopts a piecewise polytropic thermal structure with rapid transition of sub- and super-temperature gradient at the interface. In the real stars, the transition is more smooth. Direct application of the current result might be questionable. It would be worthwhile to check its validity by using smoothly varying thermal structure profiles instead of step functions. We plan to investigate these effects in the future. In addition, the flux is much smaller in real stars. We would expect more counter cells in the convectively stable zone since the penetrative velocity is smaller. Thus the cell structures in the cases with $S \geqslant 4000$ may differ significantly from those in real stars.

I thank an anonymous referee for the helpful comments and suggestions on the manuscript. I also thank K.L. Chan for the helpful discussion on overshooting, and Q.S. Zhang for his comment on the relationship between anisotropic degree and the structure of counter cells. I acknowledge the financial support from NSFC (No. 11503097,11521101), the Science and Technology Program of Guangzhou (No. 201707010006), the Guangdong Basic and Applied Basic Research Foundation (No.2019A1515011625), the Science and Technology Development Fund, Macau SAR (No. 0045/2018/AFJ), and the Independent Innovation Project of China Academy of Space Technology. The simulations were performed on the supercomputers at the Purple Mountain Observatory, and the National Supercomputer Center in Guangzhou.

Appendix

Figures 6(a)–(c) show the layer structures depicted by Zahn (1991), Zhang & Li (2012), and (Cai 2020), respectively. Zahn (1991) have used the terminology "penetration" to denote the regime where the thermal mixing is strong enough to bring the layer close to adiabaticity; and "overshooting" to denote the regime where the motions are able to mix chemicals but not strong enough to alter the thermal structure to an adiabatic state. The upper boundary of the overshooting layer is defined at the location $\mathrm{Pe} = 1$, above which the thermal dissipation dominates. The penetrative layer is also called the "nearly adiabatic layer"; and the overshooting layer is also called the "thermal adjustment layer." Based on the asymptotic analysis of a Reynolds stress model, Zhang & Li (2012) have found that an additional turbulent dissipation layer should be included in the overshooting regime. In such case, the overshooting regime contains two parts: one part that the thermal structure is gradually changed from adiabatic state to radiative state; and another part that the thermal structure is close to radiative state while the Péclet number is still greater than 1. In this paper, we use the term "thermal adjustment layer" to denote the first part, and the term "turbulent dissipation layer" to denote the second part. It should be noted that the meaning of the "thermal adjustment layer" is a little bit different between Zahn's (1991) and our work. Zahn (1991) defines the "thermal adjustment layer" as the full overshooting regime, while we define it as a part of the overshooting regime. Apart from this difference, they share the similarity that the thermal structure is gradually adjusted from adiabatic state to radiative state within this layer. The layer structure obtained in our 3D simulations is almost identical to the one depicted by Zhang & Li (2012). The major difference is that the nearly adiabatic layer is missing in the 3D simulation. Zhang & Li (2012) have shown that this layer is very thin in stars. As 3D simulation only explores a small regime in the parameter space, we cannot exclude the possibility of the existence of the nearly adiabatic layer.

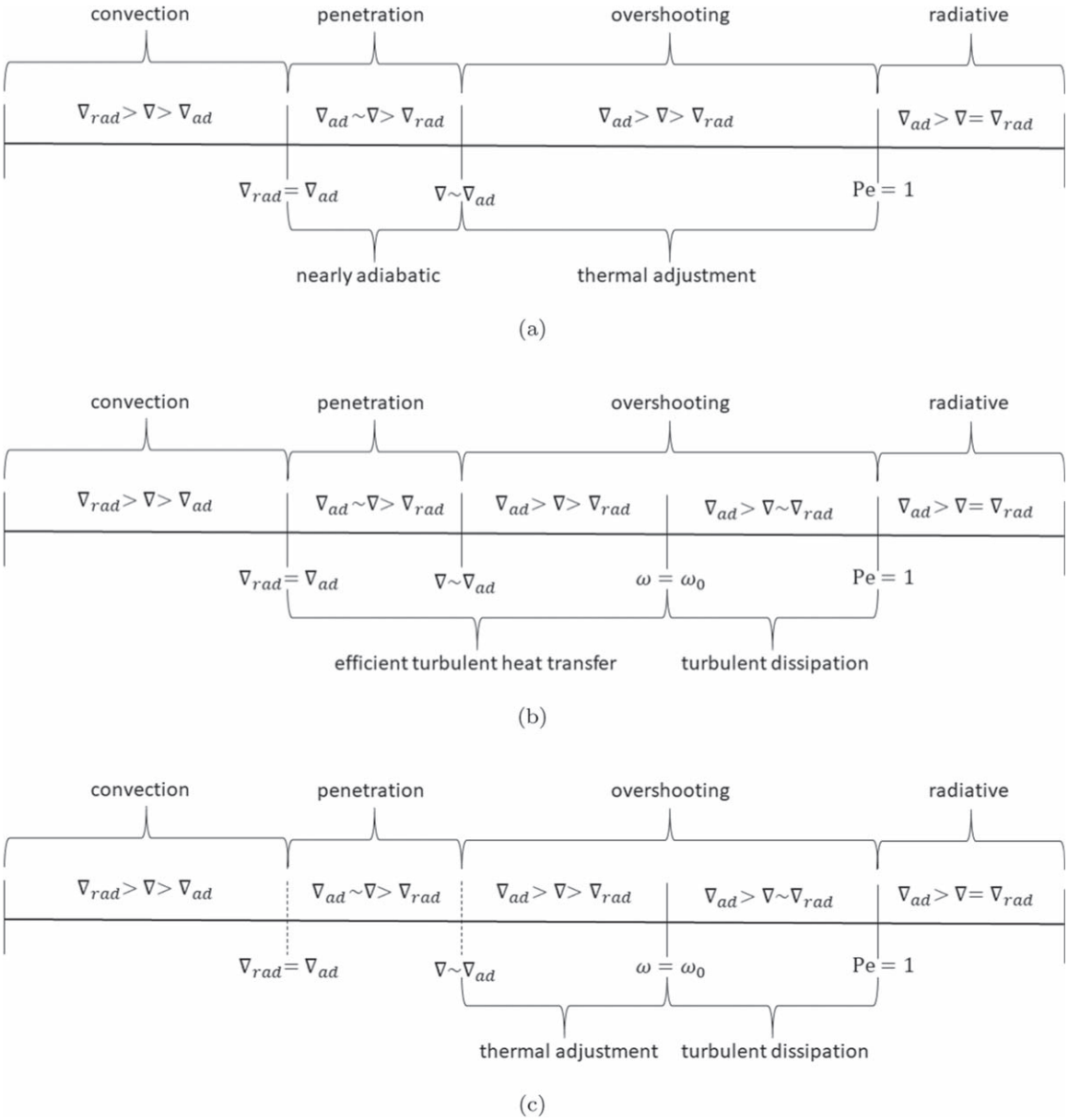

Figure 6. (a) The layer structure of Zahn (1991). (b) The layer structure of Zhang & Li (2012). (c) The layer structure of 3D simulation (Cai 2020). The region within the dashed line is missing in the 3D simulation. ω is the anisotropy of the turbulent flow, and ω_0 is an equilibrium state of ω.

ORCID iDs

Tao Cai https://orcid.org/0000-0003-3431-8570

References

Andrássy, R., & Spruit, H. 2015, A&A, 578, A106
Arnett, W. D., Meakin, C., Viallet, M., et al. 2015, ApJ, 809, 30
Brummell, N. H., Clune, T. L., & Toomre, J. 2002, ApJ, 570, 825
Cai, T. 2016, JCoPh, 310, 342
Cai, T. 2018, ApJ, 868, 12
Cai, T. 2020, ApJ, 888, 46
Chan, K. L., Cai, T., & Singh, H. P. 2010, in Proc. IAU Symp. 271, Astrophysical Dynamics: From Stars to Galaxies, ed. N. Brummell (Cambridge: Cambridge Univ. Press), 317
Claret, A., & Torres, G. 2017, ApJ, 849, 18
Claret, A., & Torres, G. 2018, ApJ, 859, 100
Claret, A., & Torres, G. 2019, ApJ, 876, 134
Deheuvels, S., Brandão, I., Aguirre, V. S., et al. 2016, A&A, 589, A93
Deng, L., & Xiong, D.-R. 2008, MNRAS, 386, 1979
Freytag, B., Ludwig, H.-G., & Steffen, M. 1996, A&A, 313, 497
Herwig, F., Bloecker, T., Schoenberner, D., & El Eid, M. 1997, A&A, 324, L81
Howard, L. N. 1961, JFM, 10, 509
Hurlburt, N. E., Toomre, J., Massaguer, J. M., & Zahn, J.-P. 1994, ApJ, 421, 245
Korre, L., Garaud, P., & Brummell, N. 2019, MNRAS, 484, 1220
Maeder, A. 1975, A&A, 40, 303
Maeder, A. 1995, A&A, 299, 84
Miles, J. W. 1961, JFM, 10, 496
Pal, P. S., Singh, H. P., Chan, K. L., & Srivastava, M. 2007, Ap&SS, 307, 399
Prat, V., & Lignières, F. 2014, A&A, 566, A110
Rogers, T., & McElwaine, J. 2017, ApJL, 848, L1
Rogers, T. M., & Glatzmaier, G. A. 2005, ApJ, 620, 432
Roxburgh, I. W. 1978, A&A, 65, 281
Shaviv, G., & Salpeter, E. E. 1973, ApJ, 184, 191
Singh, H. P., Roxburgh, I. W., & Chan, K. L. 1995, A&A, 295, 703
Woo, J.-H., & Demarque, P. 2001, AJ, 122, 1602
Zahn, J.-P. 1991, A&A, 252, 179
Zahn, J.-P. 1992, A&A, 265, 115
Zhang, Q.-S., & Li, Y. 2012, ApJ, 750, 11